



# Vertical Distribution Characteristics and Formation /Dissipation Mechanisms of Air Pollutants in Xingtai, China Based on Multi-source Data: A Case Study

Qi Jiang<sup>1,2</sup> · Fei Wang<sup>3</sup> · Zhanqing Li<sup>4</sup> · Yuan You<sup>1,2</sup> · Yuchen Jin<sup>5</sup> · Siteng Li<sup>2,6</sup> · Yele Sun<sup>7</sup> · Yingjie Zhang<sup>8</sup> · Xinrong Ren<sup>4,9</sup> · Hao He<sup>4</sup> · Russell R. Dickerson<sup>4</sup>

Received: 12 September 2024 / Accepted: 16 January 2025  
© The Author(s), under exclusive licence to Springer Nature B.V. 2025

## Abstract

The Beijing-Tianjin-Hebei urban agglomeration is one of the regions in China with the most severe air pollution. Using aircraft observations collected over Xingtai in May 2016 and multi-source data, such as aerosol chemical composition and lidar data, we analyzed aerosol composition and optical properties, vertical pollution characteristics of gases within the boundary layer, and their interactions with meteorological parameters. This study focuses on investigating the transport and evolution mechanisms of pollutants during transitions from polluted research flight No.7(RF7) to clean research flight No.8 (RF8) periods in summertime Xingtai. Results show that during RF7, the near-surface submicron aerosol (PM<sub>1</sub>) mass concentration was generally low (37.5  $\mu\text{g m}^{-3}$ ), with the contribution of inorganic salts far exceeding that of organic matter. Aircraft observations indicated weak cold-air activities above 1000 m during RF8, while the southeasterly wind still prevailed below 1000 m, with a slight increase in wind speed. From RF7 to RF8, the overall vertical atmosphere gradually transitioned from polluted to clean conditions. During RF8, an inversion layer appeared in the temperature profile between 1100 and 1300 m, with ~ 21.3% of this inversion coming from black carbon heating. Changes in meteorological and pollution transport conditions led to significant differences in PM<sub>1</sub> and gaseous components between RF7 and RF8. Compared to RF7, the contribution of nitrates decreased markedly during RF8, with the organic matter becoming the dominant component of PM<sub>1</sub>. During RF7, sulfur dioxide (SO<sub>2</sub>), nitrogen dioxide (NO<sub>2</sub>), and carbon monoxide (CO) were strongly correlated with the scattering coefficient, with correlation coefficients of 0.92 and 0.96 for SO<sub>2</sub> and NO<sub>2</sub>, respectively. By contrast, during RF8, the correlations between SO<sub>2</sub>, NO<sub>2</sub>, and CO and the scattering coefficient decreased, with SO<sub>2</sub> having the highest correlation with the scattering coefficient (coefficient of determination = 0.88). From RF7 to RF8, the concentrations of various pollutants within the boundary layer, except for ozone (O<sub>3</sub>), had decreasing trends. When the relative humidity was below 50%, O<sub>3</sub> generally contributed positively to extinction. There was no pronounced correlation between O<sub>3</sub> and relative humidity when the relative humidity exceeded 50%.

**Keywords** Boundary layer · Pollutants · Vertical observations · Chemical composition · Meteorological factors

Extended author information available on the last page of the article

## 1 Introduction

The planetary boundary layer (PBL) serves as a pivotal hub for the exchange of energy, water vapor, and matter between the surface and the atmosphere. In the PBL, physical quantities, such as wind, temperature, humidity, pressure, and turbulent diffusion, as well as chemical properties related to pollutant compositions and transformation mechanisms, vary dramatically in time and space, particularly in the vertical direction (Haskins et al. 2019; Jiang et al. 2021; Riedel et al. 2013; Sun et al. 2016b, 2020a, b). The formation and dissipation of atmospheric pollutants primarily occur within the PBL (Qu et al. 2017). The physicochemical properties and evolution mechanisms of pollutants in the vertical direction remain crucial factors affecting the accuracy of air quality forecasting models (Brook et al. 2013). Due to limitations in observation platforms and instrument resolution, existing studies on atmospheric pollution have primarily focused on ground-level measurements. It is still a complex and hot topic as to how the physical and chemical properties of the urban boundary layer interact with each other to jointly drive the formation, accumulation, and dissipation of atmospheric pollutants.

Vertical observation methods for atmospheric pollutants include comparisons of observations at different altitudes (Levin et al. 2009), meteorological tower observations, sounding balloon or tethered balloon observations (Han et al. 2018), ground-based radar observations (Wang et al. 2012), aircraft measurements (Wang et al. 2024), and model simulations (Wu et al. 2011). Each of these approaches can provide valuable insights into the vertical distribution and evolution of pollutants within the PBL. Among which, airborne instruments have been used to characterize aerosol and gas properties in the lower troposphere around the world. Although limited in terms of temporal and geographic coverage, airborne sensing can provide high resolution, direct, and in situ atmospheric pollutants observations (Wang et al. 2018a, b).

Friedrich et al. (2012) found that considering the liquid–water mixing ratio derived from the vertical humidity profile under moist-adiabatic conditions can provide a more precise determination of atmospheric stability. Zhou et al. (2018) utilized multi-source observations and numerical models to study the Yangtze River Delta region, revealing that the lifting of a cold front and the transport of pollutants facilitate the accumulation of pollutants at altitudes above 100 m rather than near the surface. Based on aircraft observations, Dong et al. (2017) demonstrated that surface cooling effects and the uneven changes in heating rates caused by absorbing aerosols altered the atmospheric temperature profile, resulting in increased stability within the PBL and instability above the PBL. The vertical variation characteristics of pollutants within the urban boundary layer are closely related to the dynamic/thermodynamic structure and turbulence characteristics of the PBL. Pollutant levels do not decrease with altitude in a straightforward manner. Aerosol mass concentrations, for example, decrease rapidly with altitude under clean weather conditions but decline more gradually in polluted or stagnant weather conditions (Ding et al. 2005). The proportion of secondary organic carbon increases with altitude, as reported by Ren et al. (2021). Simulation studies focused on the Beijing region have indicated that local sources contribute greatly to near-surface pollutants, with local contributions of nitrogen dioxide (NO<sub>2</sub>), sulfur dioxide (SO<sub>2</sub>), and the mass concentration of particulate matter with diameters less than 10 μm (PM<sub>10</sub>) reaching up to 90%, 65% and 75%, respectively. However, at an altitude of 1.1 km, the contributions from external sources (e.g., cities south of Beijing) to SO<sub>2</sub> and PM<sub>10</sub> exceed 50% (Wu et al. 2011). Studies on air pollution in Beijing have suggested that the proportion of organic matter is the highest near the surface due to surface emissions. Under polluted conditions, aerosols

are dominated by nitrates above 200 m (Sun et al. 2020a, b). At night,  $O_3$  concentrations are higher in the upper boundary layer, where the hydrolysis of dinitrogen pentoxide ( $N_2O_5$ ) to form nitrates becomes more significant. The formed nitrates contribute to increased ground-level nitrate concentrations the following day as the boundary layer mixes and develops (Sun et al. 2018).

The Beijing-Tianjin-Hebei region is located in the transition zone between mountainous and plain regions. The joint effects of blocking systems and the unique topography makes the atmospheric environment in this region highly sensitive and vulnerable to pollution (Xu et al. 2021). It is in fact one of the regions with the most severe atmospheric pollution in China (Cai et al. 2020). Xingtai, situated in southern Hebei Province, China, has a complex emission environment and high-intensity pollution emissions, making it a hotspot of air pollution in the Beijing-Tianjin-Hebei region.

Although previous studies have enhanced our understanding of the boundary layer structure and pollution mechanisms in the Beijing-Tianjin-Hebei urban agglomeration, further analysis and discussion of related issues are still needed to overcome some limitations. Specifically, there is a lack of detailed spatiotemporal observations of the boundary-layer structure, with most studies relying on low-resolution observations. Moreover, the boundary-layer structure is highly complex, with substantial differences under varying pollution conditions across different regions, thus requiring more extensive data support. In this study, we utilize aircraft observations, in conjunction with near-surface multi-source data, including submicron aerosol ( $PM_{10}$ ) chemical composition, to analyze the physicochemical and optical properties of aerosols, characteristics of the vertical variation of pollution gases in the boundary layer and their interactions with meteorological parameters. Furthermore, we focus on the transport and evolution mechanisms of a pollution-to-clean process in Xingtai during the summer, aiming to provide insights into the dynamic processes that occur during such transitions.

The remainder of this paper is organized as follows. Section 2 describes the sites and campaigns. Section 3 analyzes the results. Finally, Sect. 4 presents the main conclusions.

## 2 Sites and Campaigns

To observe vertical profiles of aerosols and gases in the North China Plain, the Air Chemistry Research in Asia campaign was conducted in Hebei Province, east of the Taihang Mountains in the North China Plain, from May to June of 2016. During the campaign, 11 vertical observation experiments were carried out using the Y-12 aircraft flying out of four local airports. The Y-12 aircraft was equipped with various instruments to measure aerosol optical properties, gas concentrations, and meteorological data. Specifically, the 550 nm aerosol scattering coefficient was measured using an integrating nephelometer (model 3565, TSI Inc.) at three wavelengths with a temporal resolution of one second. The 550 nm absorption coefficient was measured by using a particle soot absorption photometer (Radiance Research Inc., USA) with a temporal resolution of one minute. The extinction coefficient is defined as the sum of the absorption and scattering coefficients. Wang et al. (2018, 2024), Zhang et al. (2022) and Benish et al. (2020) provide detailed information about the observational instruments used in this experiment and flight trajectories. In the Xingtai region, a total of five flight experiments were conducted, referred to as RF1, RF6, RF7, RF8, and RF11. Figure 1 shows the flight trajectories of these experiments.

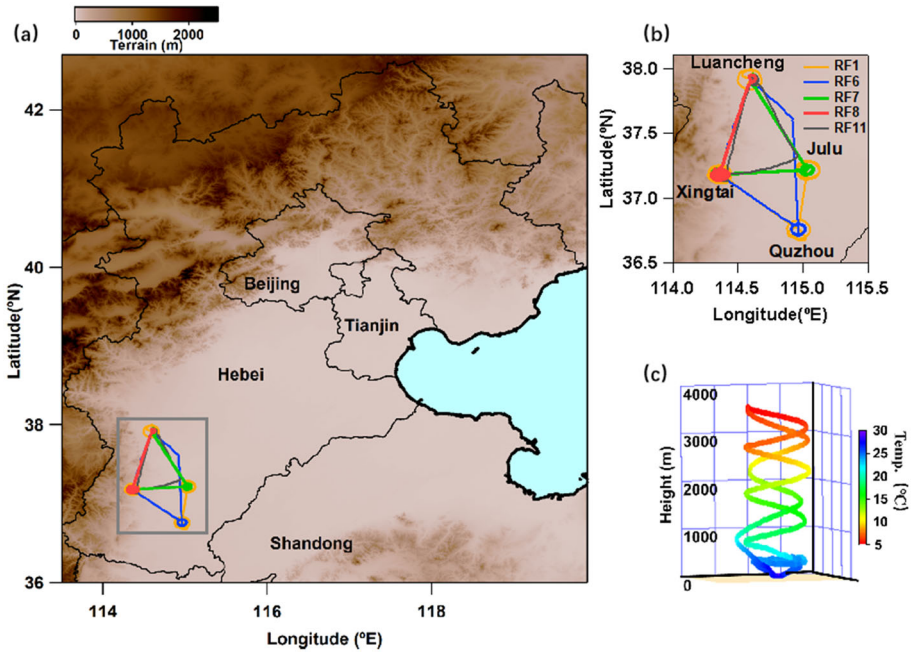


**Fig. 1** **a** Five flight trajectories over Xingtai (colored lines) with terrain elevation (in m) as the background, **b** a zoomed-in view of the flight trajectories showing the locations of the airports that the aircraft flew from, and **c** vertical legs of each flight colored by the corresponding ambient air temperature

On 28 May 2016, two aircraft observation missions were conducted over the Xingtai region, one at ~ 0300 Coordinated Universal Time (UTC, experiment RF7, 11 am local time) and the other at 0900 UTC (experiment RF8, 5 pm local time). Sky conditions, as photographed by onboard observers, were different during each observation period (Fig. 2). During the RF7 flight, the sky at an altitude of 3 km appeared grayish-yellow, with low horizontal visibility. By contrast, during the RF8 flight, the horizontal visibility at high altitudes dramatically improved, and the sky appeared bright blue.



**Fig. 2** Aerial photographs taken during the RF7 and RF8 flights

In conjunction with aircraft observations, various ground-based observations, including aerosol chemical composition and meteorological parameters, were simultaneously measured at the Xingtai supersite (114.36 °E, 37.18 °N; 182 m above sea level). Specifically, the chemical components of non-refractory PM<sub>1</sub> (NR-PM<sub>1</sub>), including sulfate (SO<sub>4</sub><sup>2-</sup>), nitrate (NO<sub>3</sub><sup>-</sup>), ammonium (NH<sub>4</sub><sup>+</sup>), chloride (Cl<sup>-</sup>), and organics (Org), were measured in situ using an Aerodyne Aerosol Chemical Speciation Monitor (ACSM) at temporal resolutions of 5–8 min (Jiang et al. 2014; Sun et al. 2020b; Zhang et al. 2018). Near-surface black carbon (BC) measurements were conducted using a seven-wavelength Aethalometer (model AE33, Magee Scientific, USA) (Drinovec et al. 2015; Wang et al. 2018a, b). The BC data used in this study were measured specifically at the 880-nm wavelength. Additionally, a Micropulse lidar (MPL, Sigma Space Corporation, USA) was deployed at the Xingtai supersite. Particle number concentrations were measured using a scanning mobility particle sizer (model 3081/3085) with a resolution of five minutes. Ground-based extinction coefficients of particulate matter were obtained from a Cavity Attenuated Phase Shift-based extinction monitor. In addition, wind profiler radar data (114.65 °E, 36.45 °N; 58 m above sea level) with a temporal resolution of six minutes were provided by the Meteorological Observation Center of the China Meteorological Administration, offering parameters such as horizontal wind speed, wind direction, and vertical velocity.

## 3 Results

### 3.1 Ground-Based Observations

Figure 3 presents PM<sub>1</sub> and its chemical components (SO<sub>4</sub><sup>2-</sup>, NO<sub>3</sub><sup>-</sup>, NH<sub>4</sub><sup>+</sup>, Cl<sup>-</sup>, organic matter, and BC), ground-level organic sources derived from the source apportionment of organic matter, meteorological elements, particle number concentrations, and the vertical backscattering coefficient obtained from the MPL on 28 May 2016. The vertical atmospheric evolution of pollutants on that day can be divided into four distinct stages, denoted as S1, S2, S3, and S4. The RF7 and RF8 flight observations occurred during stages S1 and S2, respectively. Based on MPL observations from the Xingtai supersite, we analyzed the PBL heights (PBLHs) retrieved from the normalized relative backscatter using the wavelet covariance transform method (Gamage and Hagelberg 1993) after eliminating the effects of clouds. The step size and threshold were set to 210 m and 0.05, respectively. The first value from the lower layer exceeding this threshold or falling within a given threshold interval is considered to be the micropulse lidar-derived PBLH. Li et al. (2018) provide more details.

During stage S1, the surface wind was predominantly southeasterly, and the PBLH gradually increased. Near the surface up to an altitude of 500 m, radar echoes were relatively strong, indicating notable pollutant accumulation. However, ground-level PM<sub>1</sub> mass concentrations remained relatively low at 37.5 μg m<sup>-3</sup>. The contribution of inorganic salts (NO<sub>3</sub><sup>-</sup> + SO<sub>4</sub><sup>2-</sup> + Cl<sup>-</sup> + NH<sub>4</sub><sup>+</sup>) to PM<sub>1</sub> was considerably higher than that of organic matter, especially nitrates, which accounted for ~ 28% of the total PM<sub>1</sub> composition on average. In general, high temperatures and an elevated PBLH facilitate nitrate volatilization and concentration diffusion during the daytime, especially in summer, when nitrate concentrations typically decrease significantly after sunrise. However, a noticeable peak in nitrate mass concentration was observed around 0200 UTC (10 am local time) on 28 May, surpassing the concentration of organic components. Importantly, there were no notable changes in wind direction and speed during this period, suggesting that the horizontal transport conditions of pollutants

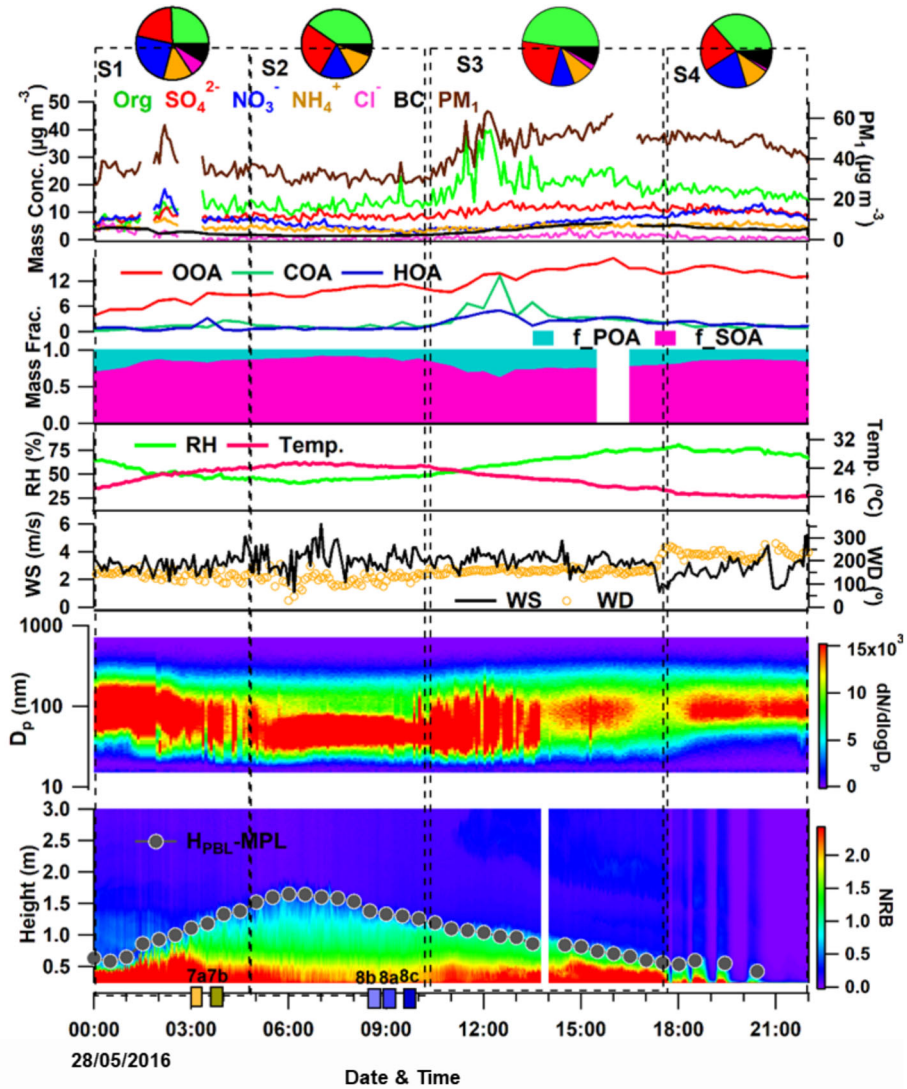


**Fig. 3** Time series of (from top to bottom) ground-level concentrations of aerosol chemical components, source apportionment of organic matter, meteorological elements, particle number concentrations, and normalized relative lidar backscatter (NRB) observations derived from the micropulse lidar (grey dots show boundary-layer heights) on 28 May 2016. Time of vertical spirals over Xingtai from RF7 and RF8 are labeled as 7a/b and 8a/b/c. Vertical dashed lines cutting through all panels represent the division of each stage (S1 – S4)

remained relatively stable. Studies on airship observations (Sun et al. 2018) and aircraft measurements (Pusede et al. 2016) have shown that regardless of pollution levels, the incremental contribution of nitrates above 200 m and higher altitudes is quite high during the nighttime. This is primarily attributed to the hydrolysis of  $N_2O_5$  (formed from the reaction between high concentrations of  $NO_2$  and  $O_3$ ) in the upper boundary layer at night, generating substantial amounts of nitrates. Around sunrise, especially from 0100 to 0200 UTC, when boundary

layer activities become more vigorous, the mixing effect becomes pronounced within the boundary layer, bringing high-concentration nitrates in the upper boundary layer down to near the surface, thereby resulting in a marked rise in the ground-level nitrate concentration. Therefore, the peak in the ground-level nitrate concentration around 0200 UTC was likely primarily due to the nitrates generated by the hydrolysis of  $\text{N}_2\text{O}_5$  in the upper boundary layer during the previous night.

Using the positive matrix factorization method (Zhang et al. 2018), three types of organic aerosols were identified: two primary organic aerosols and one secondary organic aerosol, namely, hydrocarbon-like organic aerosol, cooking-related organic aerosol and oxygenated organic aerosol. During stage S1, the oxygenated organic aerosol concentration gradually increased, and the proportion of secondary organic aerosol was over 65% of the organic matter on average, with an increasing trend. During this stage, one flight mission (RF7) with two vertical spirals (RF7a and RF7b) was conducted.

During stage S2, the near-surface wind speed increased slightly, and the wind direction fluctuated, but the prevailing wind direction remained southeasterly. MPL derived results indicate that the thickness of the pollution layer decreased substantially during stage S2, with a clear reduction in pollutant concentration in the vertical direction. Although the average ground-level  $\text{PM}_{10}$  mass concentration ( $30.6 \mu\text{g m}^{-3}$ ) decreased slightly, the overall downward trend was not pronounced. The  $\text{PM}_{10}$  chemical composition showed a significant shift between stages S1 and S2. During stage S2, the contribution of nitrates dropped sharply to 16%, while the proportion of organic matter rose substantially, becoming the dominant component of  $\text{PM}_{10}$  at 40%. Secondary organic aerosol accounted for over 90% of the organic matter. During this stage, one flight mission (RF8), comprised of three sub-missions (RF8a, RF8b, and RF8c), was conducted.

Upon entering stage S3, surface humidity gradually increased, and micropulse-lidar-derived radar echoes began to strengthen progressively in the vertical direction. Concurrently, the near-surface  $\text{PM}_{10}$  mass concentration also rose notably. In particular, the mass concentration of organic matter increased from below  $15\text{--}40 \mu\text{g m}^{-3}$  within two hours, with a growth rate of nearly  $13 \mu\text{g m}^{-3} \text{h}^{-1}$ . Studies, including those by Sun et al. (2016a, 2016b) and Wang et al. (2018), have demonstrated that as pollution intensifies, the proportion of inorganic salts increases significantly, whereas the contribution of organic matter decreases. However, during stage S3, although the mass concentration of inorganic matter increased with increasing pollution, its growth rate was much lower than that of organic matter, with the average contribution of organic matter exceeding 48% of  $\text{PM}_{10}$ . According to the source apportionment results of organic matter during this period from Zhang et al. (2018), the mass concentration of cooking-related organic aerosols began to increase considerably around 1000 UTC, reaching a peak at 1200 UTC, coinciding with the local dinner cooking time in Xingtai. The rapidly increasing cooking-related organic aerosols contributed greatly to organic matter, with a proportion of up to 40%. During this time, cooking-related organic aerosols played a crucial role in the occurrence and development of pollution in stage S3.

Upon entering stage S4, the wind direction shifted westward, and the wind speed decreased significantly. Meanwhile, the near-surface relative humidity remained at around 70%, and the ground-level  $\text{PM}_{10}$  mass concentration was slightly lower compared with stage S3. However, the proportion of inorganic salts, particularly nitrates, increased rapidly. In terms of mass concentration trends, all chemical components either decreased or remained stable after nightfall, except for nitrates, which showed a slight increase. A notable peak in nitrate mass concentration was observed from 2000 to 2100 UTC, likely driven by the shift in wind direction and the rise in wind speed. This suggests that the alteration in the pollution transport pathway was the primary influencing factor.

### 3.2 Aircraft-Based Observations of Optical Properties

The formation mechanisms of pollution can be considered from two aspects. One is the chemical reactions of internal factors, such as the formation of secondary aerosols, and the other is the impact of boundary-layer development on pollution, i.e., the external environment associated meteorological conditions for pollution (Sun et al. 2018). During the RF7b (0400 UTC) airborne sub-mission over Xingtai, the vertical distribution of the extinction coefficient clearly shows a pollution profile, with the maximum exceeding  $300 \text{ M m}^{-1}$  throughout the entire layer (Fig. 4). The wind profile (Fig. 5) reveals that from the near-surface up to 850 hPa (1500 m), southerly winds prevailed, with low wind speeds ( $< 4 \text{ m s}^{-1}$ ) and relative humidity levels of 50–60%, all favoring the development of air pollutants. Under the combined effects of terrain, emissions, and meteorological factors, the persistent southerly winds in a weak

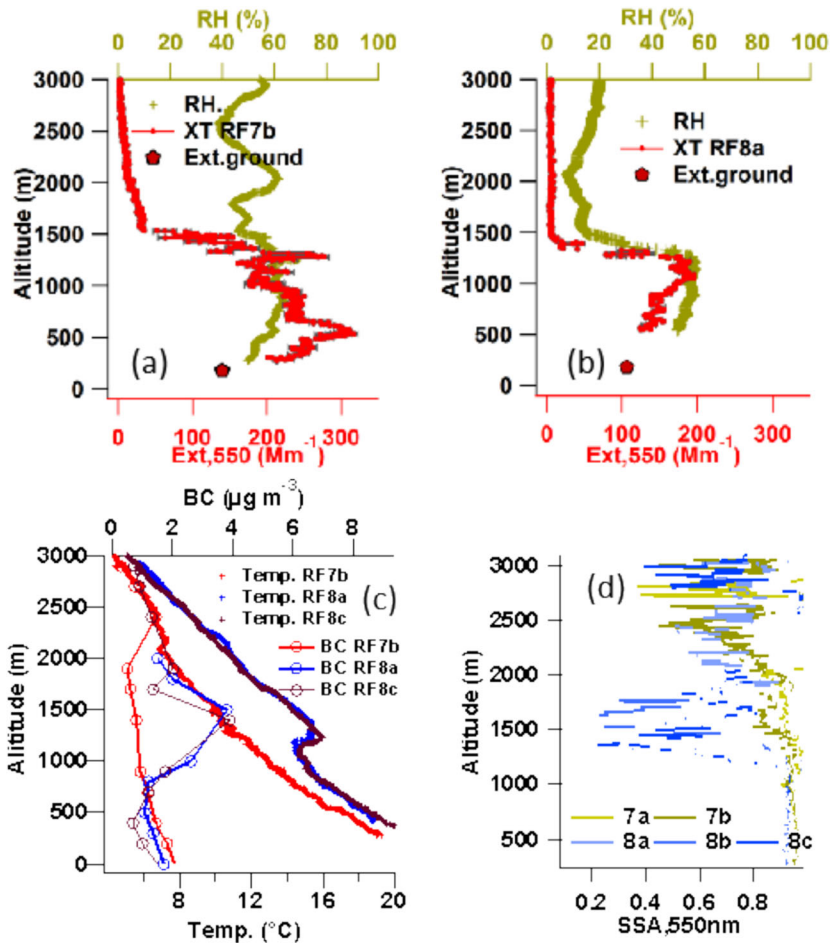


**Fig. 4** Vertical distributions of the extinction coefficient and relative humidity during **a** RF7b and **b** RF8a, **c** vertical distributions of the black carbon (BC) concentration and temperature during RF7b, RF8a, and RF8c, and **d** the vertical distribution of the single-scattering albedo during the RF7 and RF8 flights

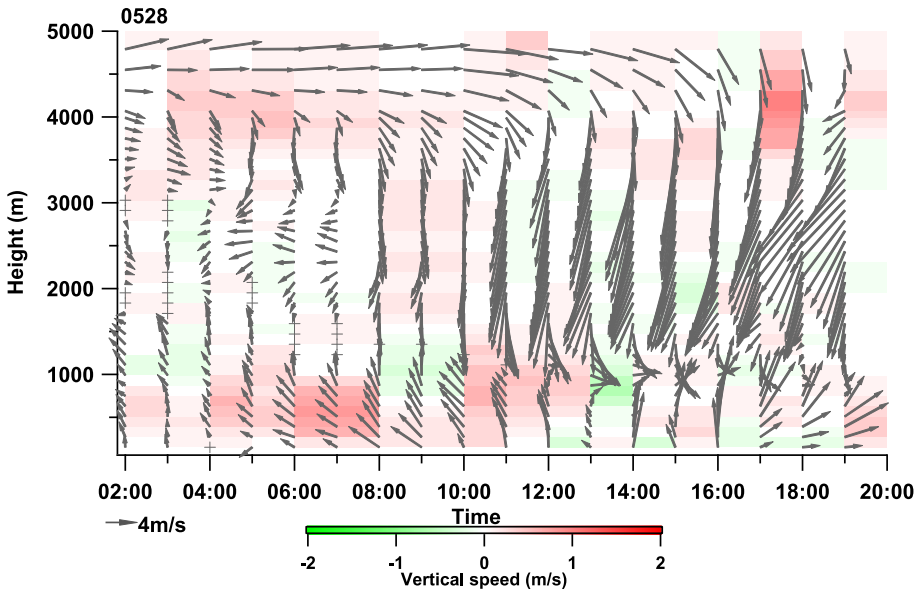


Fig. 5 Vertical wind field measured by a wind profiler radar near Xingtai on 28 May 2016

pressure field constitute a typical weather background for pollution formation in the North China Plain (Sun et al. 2018). Near the surface at that time, Xingtai was located between two high-pressure systems, which led to weak pressure gradients and horizontal diffusion. Thus, the horizontal visibility ranged from 18 to 20 km. There was no obvious inversion in the atmosphere. At 500 hPa, a cyclone positioned over eastern Inner Mongolia guided weak cold air southward. By 0200 UTC, the southern edge of the cold air had reached northern Hebei, but Xingtai was still under stagnant atmospheric conditions. Additionally, the formation of a convergence line before the arrival of cold air further contributed to pollutant accumulation in Xingtai. At around 0900 UTC (RF8), the pressure gradient at 500 hPa gradually increased as the cold vortex began to affect the Xingtai region. However, the weather system was manifested as a forward-tilting trough structure, with the wind direction shifting to northeasterly and wind speed increasing above 850 hPa. The weak cold air (northwesterly wind) primarily impacted areas above 1250 m, while southeasterly wind still prevailed below this level, with a slight increase in wind speed (including near the ground). Consistent with MPL derived results, the vertical atmosphere in the aircraft profile from RF7 (stage S1) to RF8 (stage S2) showed a transition from polluted to clean conditions, with a notable reduction in aerosol extinction. Note that the degree of reduction in the extinction coefficient varied considerably across different altitudes.

The RF8 temperature profile showed a pronounced inversion layer from 1100 to 1250 m, with a maximum inversion strength of  $0.02 \text{ } ^\circ\text{C m}^{-1}$ . Assuming that the heating rate of BC absorption in a given layer is roughly proportional to the radiation reaching that layer, the BC heating rate between 1000 and 1250 m was estimated to be  $0.049 \text{ } ^\circ\text{C h}^{-1}$  based on the BC distribution during RF8a. This estimation was made using the method proposed by Lu et al. (2020). Assuming that the maximum heating duration of BC absorption is 4 h, the maximum temperature increases in this layer due to BC heating was estimated to be  $0.20 \text{ } ^\circ\text{C}$ . The maximum inversion strength during RF8 was  $0.94 \text{ } ^\circ\text{C m}^{-1}$ , with warming due to BC

heating accounting for  $\sim 21.3\%$  of this inversion. Consequently, warm air mass activities contributed to  $\sim 78.7\%$  of the inversion at this altitude. The presence of the temperature inversion facilitated the accumulation of pollutants such as BC at this altitude (Deng et al. 2016; Han et al. 2017). The accumulation of BC, in turn, promoted the development of the inversion layer, indicating a bidirectional positive feedback effect. Due to the inversion layer, the area with large values of extinction coefficient was also concentrated in this layer. For instance, at an altitude of 1120 m, the extinction coefficient was  $186.5 \text{ M m}^{-1}$  during RF7b and  $184.8 \text{ M m}^{-1}$  during RF8a, indicating no noticeable decrease in the extinction coefficient.

Under the influence of cold air aloft, the relative humidity above the inversion layer at 1250 m during RF8a dramatically decreased. However, below the top of the inversion layer, particularly within the inversion layer, there was no remarkable decrease in water vapor content. This situation would still be conducive to the hygroscopic growth of particles and liquid-phase chemical reactions, thereby inhibiting the reduction of pollutant concentrations. Within the 1250–1500 m altitude layer above the inversion layer, the extinction coefficient decreased considerably from RF7b to RF8a due to the disturbance caused by weak cold-air activities, with the average extinction coefficient dropping from approximately  $190 \text{ M m}^{-1}$  to  $19 \text{ M m}^{-1}$ . Below the inversion layer, there was no obvious cold-air influence, and the southeasterly wind was still the prevailing wind direction. Note that observations were unavailable below 500 m in RF8a, so the 180–500 m layer was not included in the analysis. On the one hand, the slight increase in wind speed at this altitude slightly enhanced the horizontal diffusion of pollutants. On the other hand, the notable differences in the chemical composition of near-surface  $\text{PM}_{10}$  compared with RF7 (stage S1) and the fluctuations in wind direction (Fig. 3) may have caused a shift in the air mass direction during RF8 (stage S2). The section discussing the backward trajectory analysis will examine this further. As a result of these combined effects, there was also a certain decreasing trend in pollutant concentrations, but the decreasing rate was lower than that in the 1250–1500 m layer affected by weak cold-air activities. Specifically, in the 500–950 m altitude range, the aircraft-measured extinction coefficient decreased from  $\sim 271$  to  $150 \text{ M m}^{-1}$ , while the ground-based observations showed a decrease in the extinction coefficient from 140.1 to  $84.9 \text{ M m}^{-1}$ .

Table 1 presents the mean aerosol optical depth (AOD) values for different layers of the atmosphere over Xingtai during the five flights from RF7a to RF8c, calculated by integrating extinction coefficients over height (Wang et al. 2018a, b). Due to the influence of the PBL, AOD values greater than 0.1 were mainly found within the boundary layer below 2000 m. Overall AOD values recorded during RF7a and RF7b both exceeded 0.3, with values of 0.16 and 0.18 in the 0–1000 m layer, respectively, contributing over 53% to the overall AOD. During RF8, the overall AOD value was noticeably lower compared with RF7, with an

**Table 1** Mean aerosol optical depths in different layers above Xingtai during the RF7 and RF8 flights

Flights	Aerosol optical depths			
	0–1000 m	1000–2000 m	2000–3000 m	3000–4000 m
RF7a	0.16	0.14	$6.23 \times 10^{-3}$	n/a
RF7b	0.18	0.15	$6.81 \times 10^{-3}$	$4.10 \times 10^{-4}$
RF8a	0.07	0.06	$4.80 \times 10^{-3}$	$2.22 \times 10^{-4}$
RF8b	0.11	0.07	n/a	n/a
RF8c	0.10	0.05	$3.32 \times 10^{-3}$	$5.09 \times 10^{-4}$

average decrease of  $\sim 51\%$ . The single-scattering albedo, defined as the ratio of the scattering coefficient to the total extinction coefficient at a specific wavelength (Wang et al. 2018a), also varied. As the atmosphere transitioned from polluted (RF7) to relatively clean (RF8) conditions, the single-scattering albedo within the altitude range of 1250–1800 m decreased. Specifically, the average single-scattering albedo in this layer dropped from 0.85 during RF7 to 0.43 during RF8, indicating a prominent increase in the contribution of aerosol absorption to total radiation in the altitude range of 1250–1800 m. Similarly, the concentration of BC aerosols also increased significantly in this layer.

The bottom of the PBL is defined as the point where the mean decreasing rate of the aerosol scattering coefficient from aircraft measurements reaches  $\sim 0.81 \text{ M m}^{-1}$  (Wang et al. 2018a). PBLHs during RF7b and RF8a were thus identified as 1280 m and 1211 m, respectively. However, PBLHs determined by the MPL wavelet method were 1333 m and 1288 m, respectively (Fig. 3). Although the PBLH estimates obtained from the wavelet method are relatively close to aircraft observations, they are slightly overestimated. Due to the pronounced diurnal cycles of the PBL, the airborne-derived PBLH in RF7b (0200 UTC) was higher than that in RF8a (0900 UTC), as shown in Fig. 4. During heavy pollution episodes, the PBLH and meteorological conditions in the PBL play a vital role in the cumulative explosive growth and diffusion of pollutants. High aerosol concentrations can enhance the stability of the urban PBL, thereby lowering the PBLH and further exacerbating pollution, which is known as the “two-way feedback mechanism” (Ding et al. 2016; Liu et al. 2019). As the atmosphere gradually became cleaner after 0900 UTC, the changing meteorological conditions and the weakening feedback mechanism of pollutants on the PBL notably slowed down the decreasing rate of the PBLH caused by the diurnal cycle (Fig. 3).

The wind field represents the characteristics of dynamic factors within the PBL. As shown in the wind profiler radar chart (Fig. 5), after entering stage S3 at 1000 UTC, the upper-level cold air continued to descend, reaching an altitude of  $\sim 900$  m around 1300 UTC. This altitude was also the lowest level of this weak cold-air intrusion. Above 900 m, atmospheric diffusion conditions improved under the influence of the northerly wind. However, below 900 m, the southerly wind still prevailed during stage S3. After 1000 UTC, the near-surface wind speed gradually decreased, and the PBLH further decreased, causing pollutants to accumulate once again.

### 3.3 Air Mass Trajectory Analysis

The 72 h backward trajectories of air masses from 0000 to 2300 UTC on 28 May 2016 were analyzed (Fig. 6). Results reveal a shift in the direction of air masses at an altitude of 200 m between stages S2 (RF8) and S1 (RF7). During stage S2, the air masses veered easterly, originating from the heavily polluted areas of eastern Hebei and northwestern Shandong. After passing over the sea, the air masses traveled through Jiangsu, Anhui, and Henan before reaching Xingtai. The water vapor contents of the air masses increased during this journey. Compared with stage S1, the air masses during stage S2 moved noticeably faster, corresponding to a slight increase in surface wind speed during this period. In stage S2, the direction of the air masses changed, and the faster movement of air masses improved atmospheric diffusion, resulting in a slight decrease in near-surface pollutant concentrations compared with stage S1. In stage S3, the movement of air masses slowed down again, with a direction similar to that in stage S1, leading to further pollution accumulation. During stage S4, at an altitude of 200 m, there was a pronounced adjustment in the direction of pollutant transport. Specifically, air masses originated from Henan in the southwest direction, and the relative

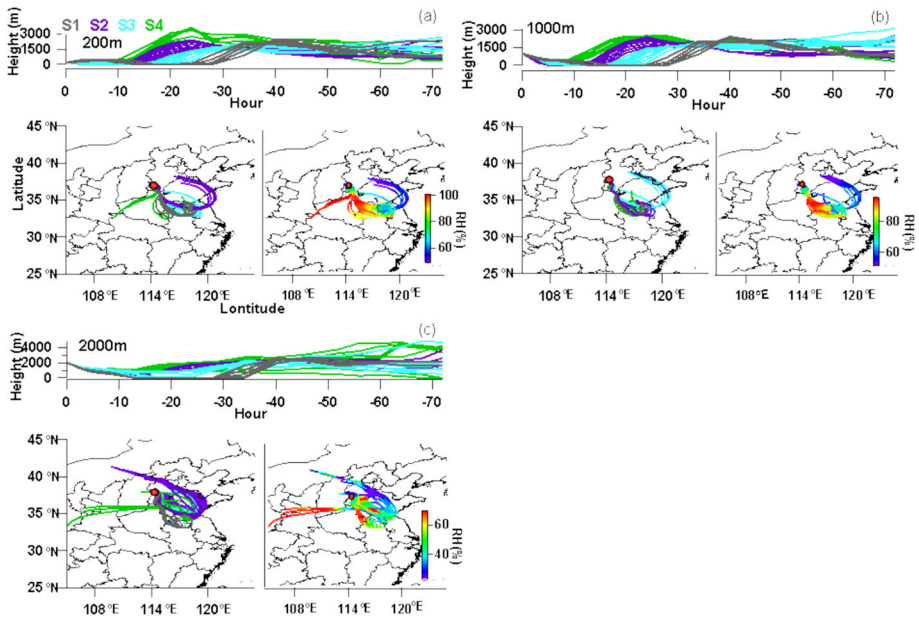


**Fig. 6** Seventy-two-hour backward trajectories at altitudes of **a** 200 m, **b** 1000 m, and **c** 2000 m from 0000 to 2300 UTC on 28 May 2016. The upper figures in panels (a–c) show 72 h backward trajectory height maps of S1–S4, the lower left figures show the origins of the backward trajectories of S1–S4, and the lower right figures show the relative humidity (unit: %) of trajectories from different origins

humidity of these air masses was relatively high, facilitating the continued development of pollution. At an altitude of 1000 m within the PBL, the air masses consistently came from the southeast across all periods, with no marked difference in pollution sources between stages S1 and S2. However, at an altitude of 2000 m above the PBL, the air mass direction in stage S1 showed no notable difference from that at lower altitudes. By contrast, during stage S2, the air masses came from the relatively clean northwestern region and moved faster, leading to a cleaner atmosphere at higher altitudes.

### 3.4 Aircraft-Based Observations of Pollutant Gases

As showed in Fig. 7, consistent with the changes in the extinction coefficient, the concentrations of various pollutants (including  $\text{SO}_2$ ,  $\text{NO}_2$ , and CO) in RF8 were noticeably lower than those in RF7, primarily concentrated below 1500 m. Above 1500 m, the concentrations of these pollutants quickly dropped to lower values as the background of the free troposphere. The trend for  $\text{O}_3$  was the opposite. Below 1500 m, the  $\text{O}_3$  concentration in RF8 was higher than that in RF7. Between 1500 and 2300 m, the  $\text{O}_3$  concentration rapidly decreased from above  $110 \mu\text{g m}^{-3}$  to  $\sim 75\text{--}82 \mu\text{g m}^{-3}$ , lower than the  $\text{O}_3$  concentration at the same altitude in RF7. Above 2300 m, there was little difference in the  $\text{O}_3$  concentration between RF7 and RF8. Notably, the  $\text{O}_3$  profile in RF7 did not rapidly decrease at any particular altitude and remained in the range between  $\sim 80$  and  $102 \mu\text{g m}^{-3}$  throughout the layer.

Gaseous and particulate pollutants from power plants, industrial emissions, and transportation contribute substantially to atmospheric extinction in the vertical direction. The

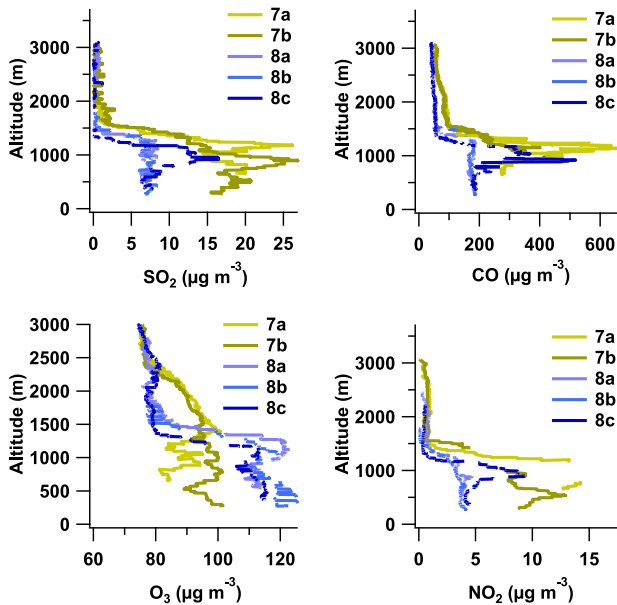


**Fig. 7** Vertical profile distributions of  $\text{SO}_2$ ,  $\text{O}_3$ ,  $\text{NO}_2$ , and  $\text{CO}$  concentrations during the RF7 and RF8 flights

correlations between pollutant gases and extinction (Figs. 8 and 9) reveal that in RF7 (representing a relatively polluted atmospheric background),  $\text{SO}_2$ ,  $\text{NO}_2$ , and  $\text{CO}$  concentrations were strongly correlated with the scattering coefficient. The correlation coefficients ( $R^2$ ) of  $\text{SO}_2$  and  $\text{NO}_2$  with the scattering coefficient were particularly high, reaching 0.92 and 0.96, respectively. However, in RF8 (representing a relatively clean atmosphere), these correlations decreased significantly. However,  $\text{SO}_2$  was still highly correlated with the scattering coefficient ( $R^2 = 0.88$ ). Unlike other pollutants, the correlation between  $\text{O}_3$  and the scattering coefficient in RF7 varied depending on the observed PBLH, which averaged 1211 m during the flight. Above the boundary layer (PBLH > 1211 m),  $\text{O}_3$  was positively correlated with the scattering coefficient ( $R^2 = 0.86$ ), with the corresponding scattering coefficients mainly ranging from 0 to  $100 \text{ M m}^{-1}$ . This suggests that in the upper atmosphere, where the influence of the boundary layer is reduced, the  $\text{O}_3$  concentration and atmospheric scattering properties were closely linked, potentially due to photochemical reactions and transport processes affecting both  $\text{O}_3$  and particulate matter. However, within the boundary layer (PBLH  $\leq 1211$  m) in RF7, as the scattering coefficient increased, the  $\text{O}_3$  concentration gradually decreased. By contrast, in the relatively clean atmosphere in RF8, the  $\text{O}_3$  concentration and the scattering coefficient showed a consistent positive correlation ( $R^2 = 0.90$ ), even higher than the correlations between other gases and the scattering coefficient during RF8. It shows  $\text{O}_3$  and  $\text{PM}_{2.5}$  (both secondary pollutants) are formed from the same emissions.

In RF7,  $\text{O}_3$  generally contributed positively to extinction at relative humidity levels below 50%. However, when the relative humidity exceeded 50%, the contribution of  $\text{O}_3$  to extinction was either positive or negative. In RF8, a similar pattern was seen, with 50% relative humidity serving as the threshold. Below this threshold, an increase in relative humidity favored  $\text{O}_3$  formation, leading to a higher  $\text{O}_3$  concentration and a corresponding rise in the scattering coefficient. Nevertheless, when the relative humidity exceeded 50%, the  $\text{O}_3$  concentration

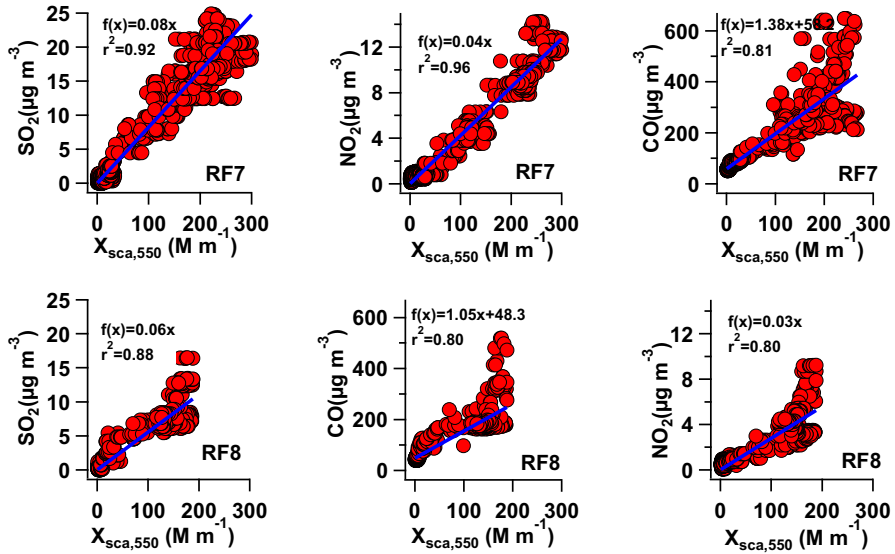


**Fig. 8** Correlations of SO<sub>2</sub>, NO<sub>2</sub>, and CO concentrations with the scattering coefficient during the RF7 (top row) and RF8 (bottom row) flights

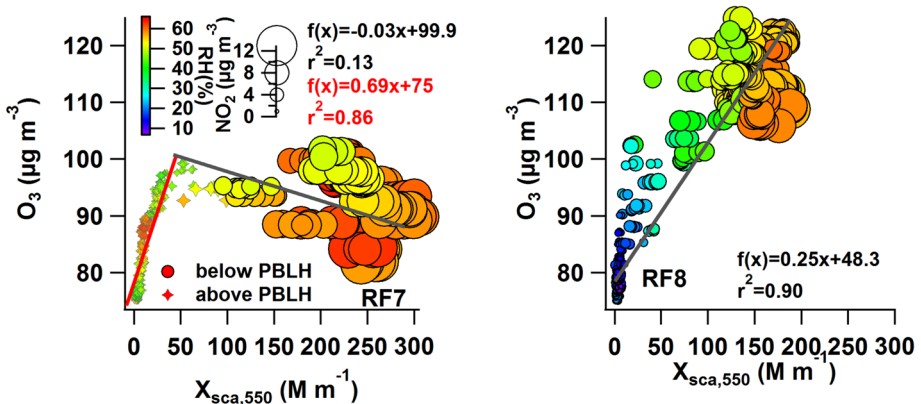


**Fig. 9** Correlations between the O<sub>3</sub> concentration and the scattering coefficient during the RF7 and RF8 flights. The circle color and size denote the relative humidity and the NO<sub>2</sub> concentration, respectively

tended to fall in the 105–125 μg m<sup>-3</sup> range. There was no apparent correlation of O<sub>3</sub> and the scattering coefficient with relative humidity.

NO<sub>2</sub> and CO can be regarded as tracers for O<sub>3</sub> pollution (Kim et al. 2013). NO<sub>2</sub> has a relatively short lifespan and primarily influences O<sub>3</sub> through photochemical reactions. The RF7 flight occurred in the morning (Beijing time), and solar ultraviolet radiation during this period is generally notably weaker compared with noon and the afternoon hours. Atmospheric pollution within the boundary layer also further weakens the amount of solar ultraviolet radiation to some extent, inhibiting the photochemical cycle of O<sub>3</sub> formation, thereby leading to the reduction and consumption of O<sub>3</sub>. This phenomenon is known as the titration effect. This

is seen during the RF7 and RF8 flights, i.e., a decrease in the  $O_3$  concentration accompanied by an increase in the  $NO_2$  concentration (Fig. 9). Due to the strong correlation between  $NO_2$  and the scattering coefficient, the extinction coefficient also showed a noticeable upward trend. CO is another important precursor of tropospheric  $O_3$ . Above the boundary layer, where nitrogen oxide concentrations are lower, and titration reactions are weaker,  $O_3$  was not noticeably consumed. This maintained the relatively high  $O_3$  concentration above the boundary layer, where the CO mass concentration in RF7 was also notably higher than that in RF8. During RF8, due to the influence of weak cold-air activities, the concentrations of all pollutants within the boundary layer, except for  $O_3$ , decreased compared with RF7. The main reason for this may be that the RF8 flight took place in the afternoon (Beijing time) when sunlight was stronger. The atmosphere during RF8 was cleaner than that during RF7, leading to a marked reduction in the atmospheric extinction capacity of pollutants. At this time, enhanced solar radiation, particularly the intense ultraviolet radiation, intensified the photochemical cycling of nitrogen oxides, thereby actively promoting  $O_3$  formation. Consequently, within the boundary layer, a positive correlation between  $O_3$  and the scattering coefficient was found. Above the boundary layer, due to the influence of weak cold-air activities, the concentrations of  $O_3$  and other gaseous pollutants decreased to relatively lower levels. However, the correlation exhibited by different gases and extinction may involve complex physicochemical mechanisms, and further corroboration with a large amount of sample data is still required.

## 4 Conclusions

Air pollution remains a significant environmental issue in China, especially in the Beijing-Tianjin-Hebei region. Detailed observations within the boundary layer are essential for accurately capturing the thermal and dynamic evolution of boundary-layer structures during pollution processes, which in turn enhances our understanding of the pollution mechanisms in the Beijing-Tianjin-Hebei region. The factors influencing pollution development can be categorized into two aspects. One involves the reactions related to the physicochemical properties of pollutants, such as the formation of secondary aerosols. The other concerns the impact of external environmental factors, such as the role of boundary-layer structures in pollution processes. For these reasons, we use aircraft observations from Xingtai in Hebei made in May 2016, combined with ground-level multi-source data, including  $PM_{10}$  chemical composition, to investigate aerosol composition and optical properties, vertical pollution characteristics of gases within the boundary layer, and their interactions with meteorological parameters. Special emphasis is placed on exploring the transport and evolution mechanisms of a pollution-to-clean transition (RF7–RF8) in the Xingtai region during the summer.

From ground-level observations, the overall  $PM_{10}$  mass concentration in stage S1 (RF7) was relatively low at  $37.5 \mu\text{g m}^{-3}$ , and the contribution of inorganic salts was considerably greater than that of organics. Upon entering stage S2 (RF8), the near-surface wind speed slightly increased, and the wind direction fluctuated to some extent, but the prevailing wind direction remained southeasterly. During stage S2, the thickness of the pollution layer noticeably decreased, and pollutant concentrations showed distinct weakening trends in the vertical direction. Although the average ground-level  $PM_{10}$  mass concentration ( $30.6 \mu\text{g m}^{-3}$ ) slightly decreased, the chemical composition of  $PM_{10}$  during stage S2 differed markedly from that during stage S1. The contribution of nitrates decreased to around 16%, while the proportion of organics gradually increased to about 40%. The contribution of secondary organic

aerosols (over 90%) was greater than that of the organics. Aircraft observations revealed that at ~ 0900 UTC (RF8), the pressure gradient at 500 hPa gradually increased as a cold vortex began to influence the Xingtai region. The primary impact of weak cold-air activities was observed above 1250 m, while below this height, the prevailing wind direction remained southeasterly, and the wind speed increased. From RF7 (stage S1) to RF8 (stage S2), the vertical atmosphere gradually transitioned from polluted to clean. In RF8, the temperature profile had a pronounced inversion at an altitude of approximately 1100–1250 m, with a maximum inversion strength of  $0.94\text{ }^{\circ}\text{C m}^{-1}$ . The warming from BC heating contributed about 21.3% of this inversion. The presence of the inversion facilitated pollutant accumulation, and the BC accumulation further promoted the development of the inversion layer, indicating a bidirectional positive feedback effect between the two. The backward trajectory analysis shows that air masses at both 2000 m and 1000 m during stage S1 came from the southeast direction. However, during stage S2, the air masses at 2000 m shifted toward the cleaner northwestern region compared with those at the same height in stage S1, moving at a faster speed, which corresponds to the transition of the upper atmosphere to a cleaner state.

Apart from the differences in  $\text{PM}_{10}$  chemical composition, there were also significant changes in the gaseous components of RF8 compared to RF7. In RF7,  $\text{SO}_2$ ,  $\text{NO}_2$ , and CO concentrations were strongly correlated with the scattering coefficient, with correlation coefficients of 0.92 and 0.96 for  $\text{SO}_2$  and  $\text{NO}_2$ , respectively. However, in RF8, these correlations dramatically decreased. However, the  $\text{SO}_2$  concentration was still relatively highly correlated with the scattering coefficient ( $R^2 = 0.88$ ). From RF7 to RF8, the concentrations of all pollutants within the boundary layer, except for  $\text{O}_3$ , had decreasing trends. Within the boundary layer,  $\text{O}_3$  concentrations gradually decreased as the scattering coefficient increased. Above the boundary layer, the  $\text{O}_3$  concentration was positively correlated with the scattering coefficient ( $R^2 = 0.86$ ), with corresponding scattering coefficients mainly ranging from 0 to  $100\text{ M m}^{-1}$ . Whether under clean (RF8) or polluted (RF7) weather conditions,  $\text{O}_3$  generally contributed positively to extinction when the relative humidity was below 50%. However, when the relative humidity exceeded 50%, the contribution of  $\text{O}_3$  to extinction was either positive or negative. There was no apparent correlation of  $\text{O}_3$  and the scattering coefficient with relative humidity.

**Acknowledgements** The authors greatly appreciate the research team and the flight crew of the Hebei Weather Modification Center for their participation in the experiment. We also acknowledge support from the CMA Key Innovation Team (CMA2022ZD10) and the WMC Innovation Team (WMC2023IT03). The reviewers are also gratefully acknowledged for their constructive comments.

**Author contributions** All authors reviewed the manuscript.

**Data availability** No datasets were generated or analysed during the current study.

## Declarations

**Conflict of interest** The authors declare no competing interests.

## References

- Benish SE, He H, Ren X, Roberts SJ, Salawitch RJ, Li Z, Wang F, Wang Y, Zhang F, Shao M, Lu S, Dickerson RR (2020) Measurement report: aircraft observations of ozone, nitrogen oxides, and volatile organic compounds over Hebei Province, China. *Atmos Chem Phys* 20:14523–14545. <https://doi.org/10.5194/acp-20-14523-2020>

- Brook JR, Makar PA, Sills DML, Hayden KL, McLaren R (2013) Exploring the nature of air quality over southwestern Ontario: main findings from the border air quality and meteorology study. *Atmos Chem Phys* 13:10461–10482. <https://doi.org/10.5194/acp-13-10461-2013>
- Cai W, Xu X, Cheng X, Wei F, Qiu X, Zhu W (2020) Impact of “blocking” structure in the troposphere on the wintertime persistent heavy air pollution in northern China. *Sci Total Environ* 741:140325. <https://doi.org/10.1016/j.scitotenv.2020.140325>
- Deng H, Tan H, Li F, Cai M, Chan PW, Xu H, Huang X, Wu D (2016) Impact of relative humidity on visibility degradation during a haze event: a case study. *Sci Total Environ* 569–570:1149–1158
- Ding G, Chan C, Gao Z, Yao W, Li Y, Cheng X, Meng Z, Yu H, Wong K, Wang S, Miao Q (2005) Vertical structures of PM<sub>10</sub> and PM<sub>2.5</sub> and their dynamical character in low atmosphere in Beijing urban areas. *Sci China Earth Sci* 48:38–54
- Ding AJ, Huang X, Nie W, Sun JN, Kerminen VM, Petäjä T, Su H, Cheng YF, Yang XQ, Wang MH (2016) Enhanced haze pollution by black carbon in megacities in China. *Geophys Res Lett* 43(6):2873–2879
- Dong Z, Li Z, Yu X, Cribb M, Li X, Dai J (2017) Opposite long-term trends in aerosols between low and high altitudes: a testimony to the aerosol–PBL feedback. *Atmos Chem Phys* 17(12):7997–8009. <https://doi.org/10.5194/acp-17-7997-2017>
- Drinovec L, Močnik G, Zotter P, Prévôt ASH, Ruckstuhl C, Coz E, Rupakheti M, Sciare J, Müller T, Wiedensohler A, Hansen ADA (2015) The “dual-spot” Aethalometer: an improved measurement of aerosol black carbon with real-time loading compensation. *Atmos Meas Tech* 8:1965–1979. <https://doi.org/10.5194/amt-8-1965-2015>
- Friedrich K, Lundquist JK, Aitken M, Kalina EA, Marshall RF (2012) Stability and turbulence in the atmospheric boundary layer: a comparison of remote sensing and tower observations. *Geophys Res Lett*. <https://doi.org/10.1029/2011GL050413>
- Gamage N, Hagelberg C (1993) Detection and analysis of microfronts and associated coherent events using localized transforms. *J Atmos Sci* 50(5):750–756
- Han S, Hao T, Zhang Y, Liu J, Li P, Cai Z, Zhang M, Wang Q, Zhang H (2017) Vertical observation and analysis on rapid formation and evolutionary mechanisms of a prolonged haze episode over central-eastern China. *Sci Total Environ* 616–617:135–146
- Han S, Hao T, Zhang Y, Liu J, Li P, Cai Z, Zhang M, Wang Q, Zhang H (2018) Vertical observation and analysis on rapid formation and evolutionary mechanisms of a prolonged haze episode over central-eastern China. *Sci Total Environ* 616–617:135–146. <https://doi.org/10.1016/j.scitotenv.2017.10.278>
- Haskins JD, Lee BH, Lopez-Hilfiker FD, Peng Q, Jaeglé L, Reeves JM (2019) Observational constraints on the formation of Cl<sub>2</sub> from the reactive uptake of ClNO<sub>2</sub> on aerosols in the polluted marine boundary layer. *J Geophys Res-Atmos* 124:8851–8869. <https://doi.org/10.1029/2019JD030627>
- Jiang Q, Sun Y, Wang Z, Yin Y (2014) Aerosol composition and sources during the Chinese spring festival: fireworks, secondary aerosol, and holiday effects. *Atmos Chem Phys* 14(14):20617–20646
- Jiang Y, Xin J, Zhao D, Jia D, Tang G, Quan J, Wang M, Dai L (2021) Analysis of differences between thermodynamic and material boundary layer structure: comparison of detection by ceilometer and microwave radiometer. *Atmos Res* 248:105179. <https://doi.org/10.1016/j.atmosres.2020.105179>
- Kim PS, Jacob DJ, Liu X, Warner JX, Yang K, Chance K, Thouret V, Nedelec P (2013) Global ozone–CO correlations from OMI and AIRS: constraints on tropospheric ozone sources. *Atmos Chem Phys* 13:9321–9335. <https://doi.org/10.5194/acp-13-9321-2013>
- Levin EJT, Kreidenweis SM, McMeeking GR, Carrico CM, Collett JL, Malm WC (2009) Aerosol physical, chemical and optical properties during the Rocky mountain airborne nitrogen and sulfur study. *Atmos Environ* 43(11):1932–1939. <https://doi.org/10.1016/j.atmosenv.2008.12.042>
- Li X, Quan JL, Wang F, Sheng J, Gao Y, Zhao D, Cheng Z (2018) Evaluation of the method for planetary boundary layer height retrieval by lidar and its application in Beijing. *Chinese J Atmos Sci (in Chinese)* 42(2):435–446. <https://doi.org/10.3878/j.issn.1006-9895.1710.17173>
- Liu L, Zhang X, Zhong J, Wang J, Yang Y (2019) The ‘two-way feedback mechanism’ between unfavorable meteorological conditions and cumulative PM<sub>2.5</sub> mass existing in polluted areas south of Beijing. *Atmos Environ* 208:1–9. <https://doi.org/10.1016/j.atmosenv.2019.02.050>
- Lu Q, Liu C, Zhao D, Zeng C, Li J, Lu C, Wang J, Zhu B (2020) Atmospheric heating rate due to black carbon aerosols: uncertainties and impact factors. *Atmos Res* 240:104891. <https://doi.org/10.1016/j.atmosres.2020.104891>
- Pusede SE, Duffey KC, Shusterman AA, Saleh A, Laughner JL, Wooldridge PJ, Zhang Q, Parworth CL, Kim H, Capps SL, Valin LC, Cappa CD, Fried A, Walega J, Nowak JB, Weinheimer AJ, Hoff RM, Berkoff TA, Beyersdorf AJ, Olson J, Crawford JH, Cohen RC (2016) On the effectiveness of nitrogen oxide reductions as a control over ammonium nitrate aerosol. *Atmos Chem Phys* 16(4):2575–2596. <https://doi.org/10.5194/acp-16-2575-2016>

- Qu Y, Han Y, Wu Y, Gao P, Wang T (2017) Study of PBLH and its correlation with particulate matter from one-year observation over Nanjing. *Southeast China Remote Sens* 9(7):668. <https://doi.org/10.3390/rs9070668>
- Ren H, Hu W, Wei L, Yue S, Zhao J, Li L, Wu L, Zhao W, Ren L, Kang M, Xie Q, Su S, Pan X, Wang Z, Sun Y, Kawamura K, Fu P (2021) Measurement report: vertical distribution of biogenic and anthropogenic secondary organic aerosols in the urban boundary layer over Beijing during late summer. *Atmos Chem Phys* 21(17):12949–12963. <https://doi.org/10.5194/acp-21-12949-2021>
- Riedel TW, Nicholas DW, Dubé WP, Middlebrook AM, Young Cora J, Öztürk F, Roya B, VandenBoer TC, Dan W, Williams EJ, Roberts JM, Steven B, Thornton AJ (2013) Chlorine activation within urban or power plant plumes: vertically resolved ClNO<sub>2</sub> and Cl<sub>2</sub> measurements from a tall tower in a polluted continental setting. *J Geophys Res-Atmos* 118(15):8702–8715. <https://doi.org/10.1002/jgrd.50637>
- Sun Y, Jiang Q, Xu Y, Ma Y, Zhang Y, Liu X, Li W, Wang F, Li J, Wang P, Li Z (2016a) Aerosol characterization over the North China Plain: haze life cycle and biomass burning impacts in summer. *J Geophys Res-Atmos* 121:2508–2521. <https://doi.org/10.1002/2015JD024261>
- Sun Y, Wei D, Fu P, Wang Q, Jie L, Ge X, Qi Z, Zhu C, Ren L, Xu W (2016b) Primary and secondary aerosols in Beijing in winter: sources, variations and processes. *Atmos Chem Phys* 16(13):1–41. <https://doi.org/10.5194/acp-16-8309-2016>
- Sun P, Nie W, Chi X, Xie Y, Huang X, Xu Z, Qi X, Xu Z, Wang L, Wang T, Zhang Q, Ding A (2018) Two years of online measurement of fine particulate nitrate in the western Yangtze River Delta: influences of thermodynamics and N<sub>2</sub>O<sub>5</sub> hydrolysis. *Atmos Chem Phys* 18(23):17177–17190. <https://doi.org/10.5194/acp-18-17177-2018>
- Sun P, Nie W, Wang T, Chi X, Huang X, Xu Z, Zhu C, Wang L, Qi X, Zhang Q, Ding A (2020a) Impact of air transport and secondary formation on haze pollution in the Yangtze River Delta: in situ online observations in Shanghai and Nanjing. *Atmos Environ* 225:117350. <https://doi.org/10.1016/j.atmosenv.2020.117350>
- Sun Y, Lei L, Zhou W, Chen C, He Y, Sun J, Li Z, Xu W, Wang Q, Ji D, Fu P, Wang Z, Worsnop DR (2020b) A chemical cocktail during the COVID-19 outbreak in Beijing, China: insights from six-year aerosol particle composition measurements during the Chinese New Year holiday. *Sci Total Environ* 742:140739. <https://doi.org/10.1016/j.scitotenv.2020.140739>
- Wang Z, Cao X, Zhang L, Notholt J, Zhou B, Liu R, Zhang B (2012) Lidar measurement of planetary boundary layer height and comparison with microwave profiling radiometer observation. *Atmos Meas Tech* 5(8):1965–1972. <https://doi.org/10.5194/amt-5-1965-2012>
- Wang F, Li Z, Ren X, Jiang Q, He H, Dickerson RR, Dong X, Lv F (2018a) Vertical distributions of aerosol optical properties during the spring 2016 ARIAs airborne campaign in the North China Plain. *Atmos Chem Phys* 18:8995–9010. <https://doi.org/10.5194/acp-18-8995-2018>
- Wang Q, Sun Y, Xu W, Du W, Zhou L, Tang G, Chen C, Cheng X, Zhao X, Ji D (2018b) Vertically-resolved characteristics of air pollution during two severe winter haze episodes in urban Beijing, China. *Atmos Chem Phys* 18:2495–2509. <https://doi.org/10.5194/acp-18-2495-2018>
- Wang F, Li Z, Jiang Q, Ren X, He H, Tang Y, Dong X, Sun Y, Dickerson RR (2024) Comparative analysis of aerosol vertical characteristics over the North China Plain based on multi-source observation data. *Remote Sens* 16(4):609. <https://doi.org/10.3390/rs16040609>
- Wu Q, Wang Z, Gbaguidi A, Gao C, Li L, Wang W (2011) A numerical study of contributions to air pollution in Beijing during CAREBeijing-2006. *Atmos Chem Phys* 11:5997–6011. <https://doi.org/10.5194/acp-11-5997-2011>
- Xu X, Cai W, Zhao T, Qiu X, Zhu W, Sun C, Yan P, Wang C, Ge F (2021) “Warm cover”: precursory strong signals for haze pollution hidden in the middle troposphere. *Atmos Chem Phys* 21(18):14131–14139. <https://doi.org/10.5194/acp-21-14131-2021>
- Zhang Y, Du W, Wang Y, Wang Q, Wang H, Zheng H, Zhang F, Shi H, Bian Y, Han Y, Fu P, Canonaco F, Prévôt ASH, Zhu T, Wang P, Li Z, Sun Y (2018) Aerosol chemistry and particle growth events at an urban downwind site in the North China Plain. *Atmos Chem Phys* 18:14637–14651. <https://doi.org/10.5194/acp-18-14637-2018>
- Zhang R, Wang Y, Li Z, Wang Z, Dickerson RR, Ren X, He H, Wang F, Gao Y, Chen X, Xu J, Cheng Y, Su H (2022) Vertical profiles of cloud condensation nuclei number concentration and its empirical estimate from aerosol optical properties over the North China Plain. *Atmos Chem Phys* 22:14879–14891. <https://doi.org/10.5194/acp-2214879-2022>
- Zhou D, Ding K, Huang X, Liu L, Liu Q, Xu Z, Jiang F, Fu C, Ding A (2018) Transport, mixing and feedback of dust, biomass burning and anthropogenic pollutants in eastern Asia: a case study. *Atmos Chem Phys* 18(22):16345–16361. <https://doi.org/10.5194/acp-18-16345-2018>

**Publisher's Note** Springer Nature remains neutral with regard to jurisdictional claims in published maps and institutional affiliations.

Springer Nature or its licensor (e.g. a society or other partner) holds exclusive rights to this article under a publishing agreement with the author(s) or other rightsholder(s); author self-archiving of the accepted manuscript version of this article is solely governed by the terms of such publishing agreement and applicable law.

## Authors and Affiliations

Qi Jiang<sup>1,2</sup> · Fei Wang<sup>3</sup> · Zhanqing Li<sup>4</sup> · Yuan You<sup>1,2</sup> · Yuchen Jin<sup>5</sup> · Siteng Li<sup>2,6</sup> · Yele Sun<sup>7</sup> · Yingjie Zhang<sup>8</sup> · Xinrong Ren<sup>4,9</sup> · Hao He<sup>4</sup> · Russell R. Dickerson<sup>4</sup>

✉ Fei Wang  
feiwang@cma.gov.cn

<sup>1</sup> National Meteorological Centre, Beijing 100081, China

<sup>2</sup> Key Laboratory of Urban Meteorology, China Meteorological Administration, Beijing 100089, China

<sup>3</sup> CMA Key Laboratory of Cloud-Precipitation Physics and Weather Modification (CPML), CMA Weather Modification Centre (WMC), Beijing 100081, China

<sup>4</sup> Department of Atmospheric and Oceanic Science, University of Maryland, College Park, MD 20742, USA

<sup>5</sup> Inner Mongolia Institute of Meteorological Sciences, Hohhot 010051, China

<sup>6</sup> Institute of Urban Meteorology, Beijing 100089, China

<sup>7</sup> State Key Laboratory of Atmospheric Boundary Layer Physics and Atmospheric Chemistry, Institute of Atmospheric Physics, Chinese Academy of Sciences, Beijing 100029, China

<sup>8</sup> School of Ecology and Nature Conservation, Beijing Forestry University, Beijing 100083, China

<sup>9</sup> Air Resources Laboratory, National Oceanic and Atmospheric Administration, College Park, MD 20740, USA